Conductivity-enhanced porous N/P co-doped metal-free carbon significantly enhances oxygen reduction kinetics for aqueous/flexible zinc-air batteries

Chuan Hu [a], Qinrui Liang [a], Yuting Yang [a], Qiming Peng [a], Zuyang Luo [a], Jiaxin Dong [a,*], Tayirjan Taylor Isimjan [b,*], Xiulin Yang [a,*]
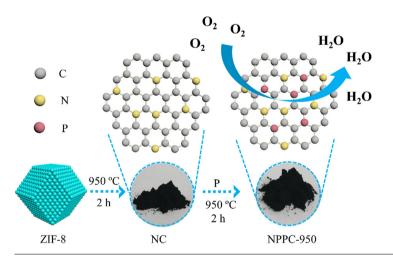
[a] Guangxi Key Laboratory of Low Carbon Energy Materials, School of Chemistry and Pharmaceutical Sciences, Guangxi Normal University, Guilin 541004, China
[b] Saudi Basic Industries Corporation (SABIC) at King Abdullah University of Science and Technology (KAUST), Thuwal 23955-6900, Saudi Arabia

HIGHLIGHTS

- Red phosphorus was calcined with MOF-derived carbon to obtain N/P co-doped carbon (NPPC-950).
- N/P heteroatom doping reduces the work function of NPPC-950 and thus promotes electron transfer.
- The P—C bond alters the charge and spin density of the C atom, thus providing more active sites.
- The catalyst showed excellent oxygen reduction performance close to Pt/C in zinc-air batteries.

GRAPHICAL ABSTRACT

A novel N/P co-doped porous carbon catalyst (NPPC-950) with high specific surface area was prepared by facile calcination method using ZIF-8 as precursor and red phosphorus as phosphorus source. The low content of P doping can significantly reduce the work function of the catalyst. The catalyst exhibits excellent oxygen reduction performance and has promising application prospect in Zinc-air batteries.

ABSTRACT

Heteroatom-doped metal-free carbon catalysts for oxygen reduction reactions have gained significant attention because of their unusual activity and economic cost. Here, a novel N/P co-doped porous carbon catalyst (NPPC) with a high surface area for oxygen reduction reaction (ORR) is constructed by a facile high-temperature calcination method employing ZIF-8 as the precursor and red phosphorus as the phosphorus source. In particular, ZIF-8 is firstly calcined to obtain N-doped carbon (NC) followed by further calcination with red phosphorus to obtain NPPC. Ultraviolet photoelectron spectroscopy (UPS) analysis shows that the ultra-low amount of P doping could significantly decrease the work function from 4.32 to 3.86 eV. The resultant catalyst exhibits a promising electrocatalytic activity with a half-wave potential ($E_{1/2}$) of 0.87 V and a limiting current density (J_L) of 5.15 mA cm^{-2}. Besides, it also shows improved

* Corresponding authors.
  E-mail addresses: chemdjx@gxnu.edu.cn (J. Dong), isimjant@sabic.com (T.T. Isimjan), xlyang@gxnu.edu.cn (X. Yang).

catalytic efficiency and excellent durability with a negligible decay of J_L after 2000 CV cycles. Moreover, aqueous and solid-state flexible zinc-air batteries (ZAB) using the catalyst show a promising application potential. This work provides new insight into developing P/N-doped metal-free carbon ORR catalysts.

1. Introduction

High performance and low-cost electrochemical oxygen reduction reaction (ORR) catalyst is critical to developing energy-efficient fuel cells and metal-air batteries [1]. The primary challenges of ORR catalyst are the complex $4e^-$ process and sluggish reaction kinetics that adversely affects the total battery's efficiency [2,3]. Throughout the research development, catalysts based on precious metals (e.g. Pt, Ir, etc.) have demonstrated outstanding performance mainly because of the faster reaction kinetics [4]. So far, many catalysts related to precious metals have been reported, including noble metal monomers, alloys, and nanoclusters [5–7]. However, precious metal catalysts still suffer from certain inherent drawbacks: 1) scarce earth reserves of precious metals and high prices, 2) weaker resistance to the toxification of reaction intermediates, and 3) poor stability [8–10]. Therefore, exploring efficient non-precious metal catalysts with low cost, high resistance to toxification, and excellent stability is the focus of research [11].

Much research has recently been devoted to finding alternatives to precious metal-based catalysts [12,13]. Among them, metal-free carbon-based catalysts stand out since carbon is sourced extensively as one of the earth's reserve-rich elements [14]. Carbon-based metal-free catalysts are primarily composed of carbon isomers with nanostructures of different dimensions [15], which feature excellent stability, large pores, high specific surface area, and excellent electrical conductivity [16]. However, pure carbon materials lack sufficient active sites and thus face low catalytic efficiency. Therefore, rational modifications of carbon materials are necessary for ORR application. Over the past decades, heteroatom-doping has been the main focus [17]. Nitrogen (N) [18], boron (B) [19], sulfur (S) [20], fluorine (F) [21], and phosphorus (P) [22] are the most commonly doped elements along with their various combinations. Studies indicate that heteroatoms can modulate the charge distribution of adjacent carbon atoms, thus changing the chemisorption mode of oxygen molecules on carbon-based materials [23,24]. Integration of elements with larger electronegativity than C (N, F, etc.) can induce charge redistribution thereby reducing the adsorption energy of the reactants/reaction intermediates [25]. In contrast, the enhanced performance evoked by doping elements that have smaller in electronegativity than C (B, P, etc.) is attributed to the electron-deficient dopant acting as a positive polarization center for O_2 [26]. The two different doping types can adjust the adsorption of *OOH and *OH intermediates [27]. In particular, the doped P atom creates unique O_2 adsorption via the side mode, thereby weakening the O—O bond via offering electrons from the P atom to the $2p^*$ orbital of O_2 [28]. Meanwhile, N doping can break the electroneutrality of carbon materials and deliver more effective adsorption sites for O_2 [29]. Compared with mono-doping, co-doping with different electronegative heteroatoms can further improve the catalytic performance, which arises from the synergistic effect caused by the electronic interactions between the dopants [30]. Some recent studies have reported that P/N co-doped metal-free carbon materials show excellent ORR activity comparable to transition metals [1,19,30,31]. The composition of the carbon material and doping manners of heteroatoms also significantly modify the catalyst performance. In addition, phosphorus-containing salts or organic molecules are the commonly used phosphorus dopants in most

studies [1,22,32–34]. Nevertheless, finding the diligent doping balances to create a unique synergy between dopants and carbon substrate thereby generating optimal ORR performance is often challenging.

Zeolite imidazole frameworks (ZIF) are the desirable precursors for preparing carbon-based catalysts featuring high conductivity and uniformly distributed active sites. In this work, we reported the construction of N/P co-doped metal-free carbon material via a high-temperature calcination method using ZIF-8 as a precursor and red phosphorus as a phosphorus source. Firstly, ZIF-8 was pyrolyzed at a high temperature to obtain NC while evaporating off the zinc and avoiding the formation of metal phosphides in the subsequent phosphating process. Secondly, the NC was ground with red phosphorus at high temperature to achieve homogeneous P doping. Thanks to the specific geometry of ZIF-8, the obtained catalyst possessed a large specific surface area and an abundance of porosity. In addition, such a phosphating method was a post-modification approach, which was simple to prepare and facilitated the material's graphitization. The as-prepared catalyst displayed good catalytic activity, excellent stability, and methanol tolerance. Furthermore, the application of such catalyst aqueous zinc-air battery (ZAB) exhibits a high-power density of 173.8 mW cm^{-2}, a high specific capacity of 800.1 mAh g$_{Zn}^{-1}$, and long stability of 300 h. Furthermore, the flexible solid-state battery applying this catalyst reached an open-circuit voltage of 1.46 V.

2. Experimental section

2.1. Materials

Zinc nitrate hexahydrate (Zn(NO$_3$)$_2$·6H$_2$O, 99%) was purchased from Sinopharm Chemical Reagent Co., Ltd. The 2-Methylimidazole (98%) was purchased from Shanghai Aladdin Biochemical Technology Co., Ltd. Methanol (CH$_3$OH, 99.5%) was purchased from Xilong Chemical Co., Ltd. Red Phosphorus (P, 98.5%) was purchased from Shanghai Aladdin Biochemical Technology Co., Ltd. All reagents were analytical grade and were used directly without further purification.

2.2. Synthesis of ZIF-8

6.5 g of 2-methylimidazole was dissolved in 80 mL of methanol, and 3 g of Zn(NO$_3$)$_2$·6H$_2$O was dissolved in 30 mL of methanol and then, the two solutions were mixed and stirred for 24 h. The white sediment was collected by centrifugation, washed three times with methanol, and dried in a desiccator at 60 °C for 12 h, obtaining ZIF-8 precursor.

2.3. Synthesis of N-doped carbon

The above-prepared ZIF-8 was placed in a high-temperature tube furnace in an Ar atmosphere and heated to 950 °C at a heating rate of 5 °C/min, held for 2 h, and then cooled to room temperature to obtain *N*-doped carbon (NC).

2.4. Synthesis of P-doped NC materials

A mixture of 20 mg NC and 20 mg red phosphorus was ground separately and placed in a high-temperature tube furnace under Ar protection and held at 850 °C, 950 °C, and 1050 °C for 2 h at a heating rate of 5 °C/min to obtain NPPC-850, NPPC-950, and NPPC-1050. As a control, the mass ratio of NC to red phosphorus was changed to 1:0.5, 1:2 and 1:3, respectively. The resulting samples were calcined at 950 °C for 2 h under Ar protection to obtain the contrast samples with different phosphorus doping contents. Besides, another 20 mg NC was calcined at 950° C for 2 h without adding red phosphorus to obtain NPC-950.

2.5. Electrochemical measurements

All electrochemical experiments were performed by an electrochemical workstation (CHI 760E) in an aqueous electrolyte of 0.1 M KOH saturated with oxygen and nitrogen. The three-electrode system consists of a rotating disk electrode (RDE, area: 0.196 cm^{-2}) or rotating ring disk electrode (RRDE, disk area: 0.247 cm^{-2}, ring area: 0.187 cm^{-2}) as the working electrode, a graphite plate as the counter electrode, and an Ag/AgCl electrode as the reference electrode. The catalysts ink was prepared by mixing 1 mg catalysts, 195 μL isopropanol, and 5 μL Nafion (10 %) water solution. And then, 16 μL of well-dispersed ink was slowly dropped on the RDE (20 μL for RRDE). For comparison, the commercial Pt/C electrode was prepared by the same method. All tests were performed using RDE except for the hydrogen peroxide yield test using RRDE. Cyclic voltammetry (CV) measurements were performed in O$_2$/N$_2$-saturated 0.1 M KOH solution with a potential range of $-$ 0.9 $\sim$ 0. 2 V versus the reference electrode at a scan rate of 50 mV s^{-1}. Linear sweep voltammetry (LSV) curves were recorded in O$_2$/N$_2$-saturated solution at a scan rate of 10 mV s^{-1} for different rotating speeds from 400 to 2025 rpm, respectively. The applied potential vs. Ag/AgCl (3 M KCl) was converted to reversible hydrogen electrode (RHE) potential using the following equation [35]:

$$E_{RHE} = E_{Ag/AgCl} + 0.059pH + E_{Ag/AgCl}^{\ominus} \qquad (1)$$

where E$_{Ag/AgCl}$ was the experimentally measured potential using Ag/AgCl as the reference electrode and E$_{Ag/AgCl}^{\ominus}$ was 0.197 V.

The average number of electrons transferred (n) per oxygen molecule was calculated according to the following Koutechy-Levich (K-L) equation [36]:

$$\frac{1}{J} = \frac{1}{J_L} + \frac{1}{J_K} = \frac{1}{B\omega^{1/2}} + \frac{1}{J_K} \qquad (2)$$

$$B = 0.62nFC_0 v^{-1/6}D_0^{2/3} \qquad (3)$$

$$J_K = nFkC_0 \qquad (4)$$

where J, J_K, and J_L are the measured, kinetic, and diffusion limiting current densities, respectively. The ω is the angular velocity of the rotating electrode (rad s^{-1}), F is the Faraday constant (F = 96485 C mol^{-1}), C_0 is the concentration of O$_2$ in 0.1 M KOH (1.21 $\times$ 10^{-3} M), D_0 is the diffusion coefficient of O$_2$ in 0.1 M KOH (1.9 $\times$ 10^{-5} cm^2 s^{-1}), v is the kinematic viscosity of the electrolyte (0.01 cm^2 s^{-1}), and k is the electron transfer rate constant.

The electron transfer number (n) and hydrogen peroxide yield (H$_2$O$_2$%) were calculated by the following equations [37]:

$$n = \frac{4I_D}{I_D + I_R/N} \qquad (5)$$

$$H_2O_2 (\%) = \frac{200I_R/N}{I_D + I_R/N} \qquad (6)$$

where I_D and I_R represent the disk and ring currents, respectively, and N is the ring collection coefficient determined to be 0.37.

2.6. Aqueous Zinc-air battery tests

The catalyst ink was prepared by dispersing 2 mg catalyst into 390 μL isopropanol solution containing 10 μL Nafion and ultrasonicated well. Then, the entire catalysts ink was sprayed onto a carbon fiber paper and controlled the catalyst coating with an area of approx. 1 cm^2. The Pt/C electrode was prepared in the same method. The carbon paper, a Zn foil and a 6 M KOH solution containing 0.2 M Zn(Ac)$_2$ were used as air cathode, anode and electrolyte, respectively. The open circuit voltage and polarization curves were obtained by CHI 760E, and the other tests were conducted by the LAND battery test system (BT2016A). Polarization curves (I-V) were collected using LSV with a voltage range from open circuit voltage to 0.4 V at a scan rate of 10 mV s^{-1}. The power densities were calculated by the following equation [37]:

$$P = U \times I \qquad (7)$$

where P is the discharge power density (mW cm^{-2}), U is the discharge voltage (V), and I is the discharge current density (mA cm^{-2}).

The specific capacity was also measured at the current densities of 10 mA cm^{-2}. The charging-discharging tests were carried out at a current density of 5 mA cm^{-2} and 20 min per cycle.

2.7. Solid-state flexible batteries tests

The catalyst ink was prepared in the same way as the zinc-air battery. Carbon cloth coated with a catalyst, zinc foil and polyvinyl alcohol hydrogel (PVA gel) electrolyte as cathode, anode, and solid electrolyte, respectively. The solid-state electrolyte was synthesized by following the process. First, 5 g of polyvinyl alcohol (PVA) was added to 40 mL of deionized water and stirred at 90 °C for 1 h. Subsequently, 10 mL 9 M KOH solution containing 0.2 M Zn(Ac)$_2$ was added to the above solution and stirred for another 0.5 h. Finally, the resulting paste was poured into a flat container and formed a film of approximately 1 mm thickness. The film was frozen overnight at $-$ 10 °C to obtain the solid-state electrolyte. All tests were similar to aqueous zinc-air battery tests.

2.8. Materials characterization

The microscopic surface morphology and ultrastructure of the prepared material were investigated by scanning electron microscopy (SEM, FEI Quanta 600) and transmission electron microscopy (TEM, JEOL, JEM-2100F). X-ray diffraction (XRD) was carried out by using a Rigaku D/MAX 2500 v/pc (Japan) diffractometer with Cu Kα radiation. The chemical valence state of each element was analyzed by X-ray photoelectron spectroscopy (XPS, Thermo Fisher Scientific NEXSA). Ultraviolet photoelectron spectroscopy (UPS) was carried out by X-ray photoelectron spectroscopy (PHI5000 VersaProbe III). The Brunauer analyzed specific surface area and pore size–Emmett–Teller (BET, 3H-2000PS4) and Barrett–Joyner–Halenda (BJH) methods. Defects and graphitization degree were analyzed in Via confocal Raman spectroscopy (Renishaw, England).

3. Results and discissions

3.1. Synthesis strategy and physical characterization

As shown in Fig. 1a, ZIF-8 was first synthesized in methanol solution by stirring at ambient temperature. Then, the as-
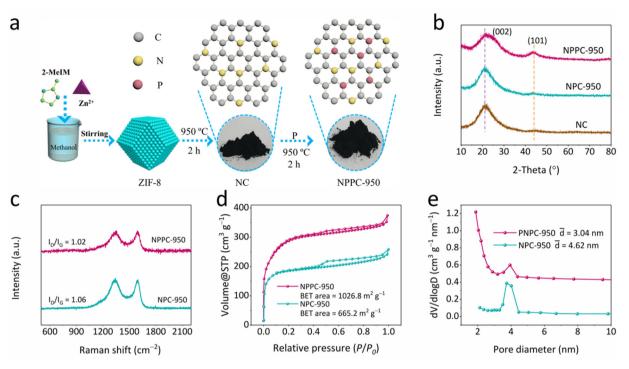
Fig. 1. (a) The synthesis schematic diagram of NPPC-950. (b) XRD patterns of NC, NPC-950 and NPPC-950. (c) Raman spectra of NPC-950 and NPPC-950. (d) N₂ isotherm adsorption–desorption curves and (e) pore size distribution curves of NPPC-950 and NPC-950.

prepared ZIF-8 was calcined at 950 °C under argon protection, obtaining nitrogen-doped carbon intermediate (NC). Finally, NC was mixed with phosphorus powder and ground well for the second calcination in argon protection at 950 °C to obtain N/P co-doped porous carbon (NPPC-950). As a control, NC was calcined under the same conditions except for the addition of red phosphorus to obtain NPC-950. X-ray diffraction (XRD) analysis revealed that NPPC-950, NPC-950, and NC all displayed two broad "humps" at 22° and 44° in XRD patterns (Fig. 1**b**), attributing to (0 0 2) and (1 0 1) planes of graphitic carbon, respectively [38,39]. Meanwhile, the control samples at different phosphating temperatures exhibited the same XRD characteristic peaks of graphitic carbon, indicating that all the obtained samples were typical carbon-based metal-free materials. Raman analysis further found that all samples showed two peaks in Raman spectra (Fig. 1**c**), where the D-band (disordered graphitic structures) at 1340 cm^{-1} and the G-band (vibration of the sp^2 hybridized carbon) at 1590 cm^{-1} [40]. The intensity ratio (I_D/I_G) of NPC-950 and NPPC-950 was calculated to be 1.06 and 1.02, showing that the degree of graphitization of the materials increased slightly with the incorporation of P. The effect of P incorporation on the specific surface and porosity of the material was studied by Brunauer–Emmett–Teller (BET) analytical technique. As shown in Fig. 1**d**, both the N₂ adsorption–desorption isotherms revealed a typical type IV curve with a H₃-type hysteresis loop, reflecting the presence of mesopores, which can expose more active sites during the process of ORR [41]. The measured BET surface area of NPPC-950 and NPC-950 were 1026.8 and 665.2 m^2 g^{-1}. The calculated average pore size by Barrett–Joyner–Halenda (BJH) model was approximately 3.04 and 4.62 nm, respectively (Fig. 1**e**). The result suggested that incorporating P increased the specific surface of the material dramatically while reducing the average pore size. It showed that this phosphating method significantly changed the pore structure.

The morphology of NPPC-950 was identified by scanning electron microscopy (SEM) and transmission electron microscopy (TEM). As depicted in Fig. 2**a**, the SEM image illustrated the irregular rod-shaped structure of NPPC-950, which is cross-linked with each other and with particle sizes ranging from 200 ~ 300 nm. Furthermore, the fine microstructure was illustrated by the TEM and high-resolution transmission electron microscopy (HR-TEM). TEM and HR-TEM images revealed the homogeneous textured amorphous carbon structure of NPPC-950 (Fig. 2**b-c**). High angle annular dark field transmission electron microscope (HAADF-TEM) image and the corresponding energy dispersive spectrometer (EDS) element mappings demonstrated a homogeneous distribution of C, N, and P elements, indicating the successful doping of N/P elements (Fig. 2**d**). We adopt the phosphorization method of mixing and grinding pre-prepared nitrogen-doped carbon powder with red phosphorus powder and then calcining at a high temperature. This approach will inevitably lead to inhomogeneous mixing at the microscopic level. Therefore, the calcination process can lead to a higher density of P doping in a few particular areas due to the non-uniform distribution of red phosphorus powder.

X-ray photoelectron (XPS) measurement analyzed these materials' surface chemical compositions and chemical states. At first, the XPS survey spectrum shows the presence of elements C, N and O on the surfaces of NPPC-950 and NPC-950 (Fig. 3**a**). The imperceptible P signal in NPPC-950 stemmed from its tiny doping amount, with a surface content of 1.10 at% (**Table S1**). As shown in Fig. 3**b**, the high-resolution spectra of C 1*s* of NPPC-950 and NPC-950 were deconvoluted into four peaks at 284.0, 284.8, 286.0, and 289.6 eV, which were assigned to C=C, C—C/C—N, C—O, and C=O bonds [1], respectively. High resolutions of N 1 *s* peaks (Fig. 3**c**) of NPPC-950 and NPC-950 showed that both could be divided into pyridinic-N (397.62 eV), pyrrolic-N (399.16 eV), graphitic-N (400.47 eV), and oxidized-N (402.16 eV) [42]. After phosphorus doping, the pyridine- and pyrrole-N contents in NPPC-950 were almost identical to NPC-950, but the graphite-N content was reduced. In Fig. 3**d**, the high-resolution P 2*p* spectrum of NPPC-950 showed three deconvoluted peaks of P — C (132.31 eV), P — N (134.30 eV), and P — C (136.23 eV) [43,44]. These peak areas' proportions showed that P—O and P—C were predominant. Moreover, the presence of P—C and P—N bonds also demonstrated the successful doping of phosphorus. In addition, ultraviolet photo-
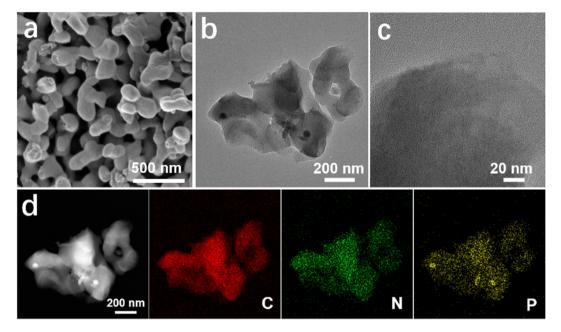
Fig. 2. (a) SEM image, (b) TEM image, (c) HR-TEM image and (d) HAADF-TEM image and corresponding EDS element mappings of NPPC-950.
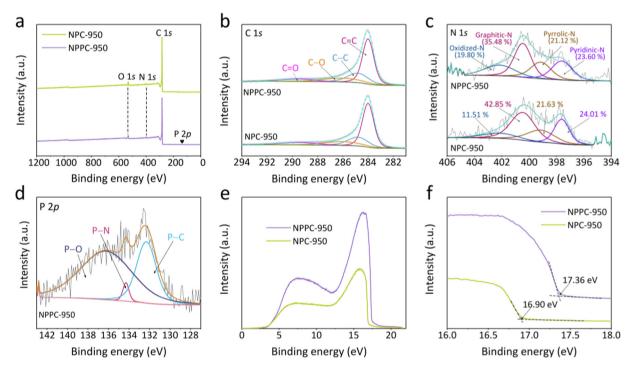

Fig. 3. (a) XPS survey spectra of NPPC-950 and NPC-950. (b) High-resolution C 1s, and (c) N 1s XPS spectra of NPPC-950 and NPC-950. (d) High-resolution P 2p XPS spectra of NPPC-950. (e) UPS spectra of NPPC-950 and NPC-950 using a He I (21.22 eV) radiation. (f) Secondary electron cutoffs (E_{cutoff}) of NPPC-950 and NPC-950.

electron spectroscopy (UPS) measurement has been used to investigate the effect of phosphorus doping on the internal electronic structure information and work function of the catalysts. As shown in Fig. 3e, two distinguished regions can be assigned to $\pi+\delta$ and δ bonds in the carbon matrix, respectively [20]. It can be observed that after P doping, NPPC-950 possessed the highest intensity of $\pi+\delta$ and δ, which indicated that the incorporation of P elements could significantly modulate the electronic structure in the carbon matrix. Fig. 3f shows the secondary electron cutoffs (E_{cutoff}) of NPPC-950 and NPC-950, which were 17.36 and 16.90 eV, respectively. Furthermore, the work function (WF) of NPPC-950 and

NPC-950 were 3.86 and 4.32 eV, respectively, while the WF indicates the minimum energy barrier required for an internal electron to escape from the nucleus. The lower WF of NPPC-950 suggested a smaller energetic barrier for transferring electrons from the catalyst surface to adsorbed molecular oxygen [45].

3.2. Oxygen reduction performance evaluation

The electrocatalytic activities of resultant catalysts were assessed by rotating disk electrode (RDE) and rotating ring disk electrode (RRDE) in O₂– and N₂-saturated 0.1 M KOH solution.

All the measured potentials were converted relative to reversible hydrogen electrode (RHE). Fig. S1a shows the cyclic voltammetry (CV) curves at various phosphating temperatures. The NPPC-950 and the NPPC-1050 exhibited identical cathodic reduction peak positions but were more positive than the NPPC-850. The linear sweep voltammetry (LSV) polarization curves showed that the NPPC-950 and the NPPC-1050 exhibited a more positive half-wave potential ($E_{1/2}$) than NPPC-850. At the same time, the difference between NPPC-950 and NPPC-1050 was insignificant, demonstrating that higher phosphating temperatures (950 °C, 1050 °C) were advantageous in conferring better catalytic activity (Fig. S1b), while the smaller temperature differences gave an inconspicuous effect on the catalytic performance. Therefore, 950 °C was the optimal temperature. We also investigated the effect of high-temperature phosphorylation of NC with different masses of red phosphorus on the catalytic performance, and the results are supplemented in **Fig. S2**. The results show that the best catalytic performance was exhibited at a mass ratio of 1:1 between NC and red phosphorus. And neither too little (1:0.5) nor too more (1:2, 1:3) red phosphorus can effectively improve the activity of the catalyst. As shown in **Fig. S3**, the CV curves of both mono- and co-doped catalysts exhibited a well-defined ORR cathodic peak, revealing an apparent oxygen reduction behavior. The N/P

co-doped catalyst (NPPC-950) provided a more positive reduction peak than the *N*-doped catalyst (NPC-950), implying that NPPC-950 possessed superior ORR activity. The LSV tests further revealed that the $E_{1/2}$ of NPPC-950 is 0.87 V, higher than NPC-950 (0.82 V) but close to that of Pt/C (0.88 V). Furthermore, the limiting current density (J_L) reached 5.15 mA cm^{-2}, more significant than that of NPC-950 (3.9 mA cm^{-2}) (Fig. 4**a**), which further demonstrated that P incorporation significantly induced an enhancement of the catalytic activity of NPC-950. Compared to other recently reported metal-free or metal-based catalysts, NPPC-950 exhibited competitive advantages (Fig. 4**b** and **Table S2**). An ORR process involved multi-step electron transfer pathways containing O*, OH*, and OOH* intermediates. So, the electron transfer number (n) was a chemical descriptor to clarify the catalytic mechanism [41]. Here, we collected LSV curves for NPPC-950 at different rotational speeds using RDE (Fig. 4**c**). The Koutecky–Levich (K–L) plots obtained based on the polarization curves exhibited apparent linearity, implying that NPPC-950 follows first-order reaction kinetics in ORR [46]. And the electron transfer numbers n of NPPC-950 determined by the K–L plots was 4.08, indicating that oxygen was predominantly reduced to water through a desirable four-electron reduction pathway [47]. Next, RRDE measurement was carried out to confirm these catalysts' actual n. These catalysts' disk and
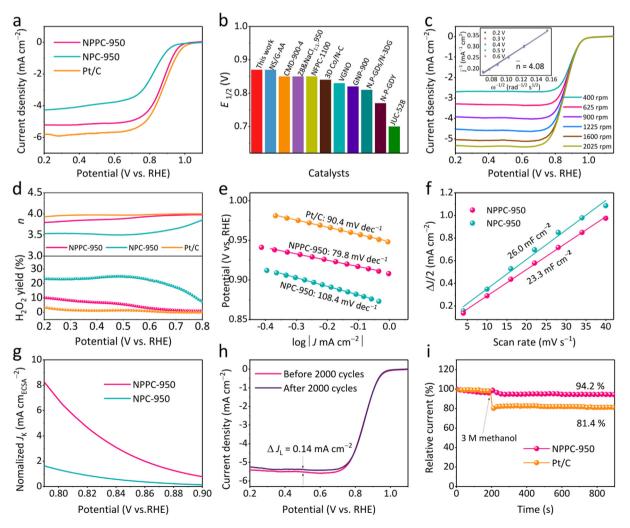

Fig. 4. (a) RDE LSV polarization curves of different catalysts. (b) Comparison of the activity ($E_{1/2}$) for NPPC-950 and other reported catalysts. (c) ORR polarization curves of NPPC-950 at various rotations. (d) The H$_2$O$_2$ yield (%) and electron transfer numbers (n) of different catalysts. (e) Tafel plots of different catalysts abstracted from LSV curves. (f) The fitting plots of C_{dl}. (g) Kinetic current density curves normalized to ECSA for different catalysts. (h) LSV polarization curves at 1600 rpm of NPPC-950 before and after 2000 CV cycles. All tests were conducted in 0.1 M KOH solution. (i) The methanol crossover effect test of NPPC-950 and Pt/C.

ring currents were collected, as shown in **Fig. S4**. According to disk and ring currents, the calculated n of NPPC-950 was close to 4, and the H_2O_2 yield (%) was less than 10 %, comparable to that of commercial Pt/C (Fig. 4**d**), further emphasizing a quasi-four-electron transfer pathway. In addition, the Tafel slopes of these catalysts were calculated to determine the reaction kinetics [48]. The Tafel slope of NPPC-950 (79.8 mV dec^{-1}) is much less than NPC-950 (108.4 mV dec^{-1}) (Fig. 4**e**), indicating its faster reaction kinetics [49].

Double-layer capacitance (C_{dl}) and electrochemical surface areas (ECSA) were measured to estimate the effective contact area between electrolyte and catalyst. The C_{dl} value of NPPC-950 was 23.3 mF cm^{-2}, lowing than that of NPC-950 (26.0 mF cm^{-2}) (Fig. 4**f** and **Fig. S5**). The smaller pore size of NPPC-950 could result from the structural collapsing generated by higher-level distortion caused by the P doping due to the oversized atomic radios. Furthermore, the ECSA values of these catalysts were measured by K_3[Fe(CN)$_6$] experiment (**Fig. S6**). As expected, NPPC-950 (0.83 m^2 g^{-1}) again possessed a smaller ECSA than that of NPC-950 (1.11 m^2 g^{-1}), following the changing pattern of C_{dl}. Generally, a larger ECSA contributes to an effective electrode–electrolyte interface area and exposes more active sites [50]. But, the better intrinsic activity of the active sites can also impart efficient catalytic activity. To further validate this point, we normalized the kinetic current density (J_K) by ECSA. As shown in Fig. 4**g**, the normalized J_K for NPPC-950 was much greater than that for NPC-950, demonstrating the higher catalytic efficiency of the active sites of NPPC-950 [51]. As a result, the overall catalytic performance of NPPC-950 is still much better than that of NPC-950, regardless of the lower ECSA. Moreover, the long-term durability of NPPC-950 was evaluated by an accelerated stability test between 0.65 and 1.05 V versus RHE at 100 mV s^{-1} in

O$_2$-saturated 0.1 M KOH. As depicted in Fig. 4**h**, the NPPC-950 showed a slight J_L decay of 0.14 mA cm^{-2} and an unchanged $E_{1/2}$ after 2000 CV cycles, indicating superior durability during ORR. Chronoamperometry measurement was used to assess methanol tolerance of NPPC-950 and Pt/C. A constant voltage was applied to the electrode at 1600 rpm in 0.1 M KOH solution. When the reaction reaches 200 s, a certain amount of anhydrous methanol is quickly poured into the electrolyte to keep the methanol concentration in the solution at about 3 M. After adding methanol, NPPC-950 retained 94.2% of the initial current, while Pt/C only retained 81.4% under the same condition (Fig. 4**i**), indicating a higher methanol tolerance of NPPC-950 than Pt/C.

TEM characterization of NPPC-950 after 2000 cycles of cyclic voltammetry testing revealed that such carbon structures showed no obvious corrosion (Fig. 5**a-b**). Furthermore, the EDS elemental mapping demonstrated that the C, N, and P were homogeneously dispersed throughout the catalyst (Fig. 5**c**), demonstrating the structural stability of NPPC-950. XPS analysis was performed on NPPC-950 after 2000 CV cycles. The C 1s spectra were presented in **Fig. S7**. As shown in Fig. 5**d**, the relative contents of pyridinic-N and graphitic-N decreased, while pyrrolic-N increased. Meanwhile, only the P—C bond was detected (Fig. 5**e**), and there was no significant decline in the performance. The results indicate that the pyrrolic-N and P—C are the two critical components for higher ORR performance.

3.3. Zinc-air battery tests

The NPPC-950 has been applied to an aqueous Zn–air battery (ZAB) as a cathode catalyst, given its excellent ORR performance. The schematic of assembled rechargeable aqueous ZAB is illus-
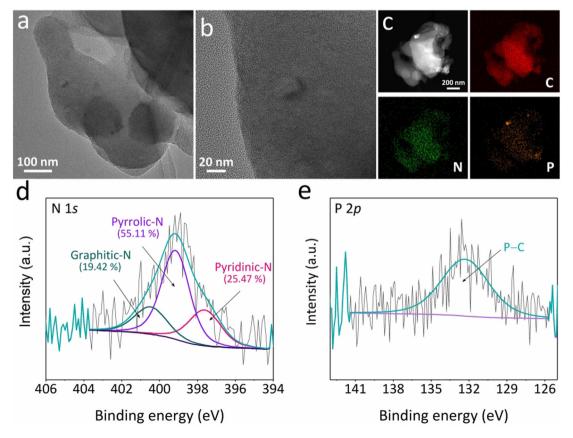

Fig. 5. (a), (b) TEM images, and (c) HAADF-TEM image and corresponding EDS element mapping of NPPC-950 after 2000 CV cycles. (d) High-resolution N 1*s* and (e) P 2*p* XPS spectra of NPPC-950 after 2000 CV cycles.

trated in Fig. 6**a**. The as-prepared catalyst was fixed on hydropho-
bic carbon paper as an air electrode, a Zn foil acted as an anode, and
assembled with the electrolyte containing 6 M KOH and 0.2 M Zn
(Ac)$_2$. As presented in Fig. 6**b**, the NPPC-950 ZAB exhibited a higher
open-circuit voltage (OCV) of 1.53 V than Pt/C ZAB (1.44 V). The
discharge/charge polarization and power density curves are shown
in Fig. 6**c**, as can be seen that NPPC-950 ZAB achieved a peak power
density of 173.8 mW cm^{-2} at 276 mA cm^{-2}, surpassing that of Pt/C
ZAB (136.1 mW cm^{-2} at 170 mA cm^{-2}). Even some reported metal-
based catalysts (Fig. 6**d** and **Table S3**). Discharge plots obtained at a
constant current density of 10 mA cm^{-2} were used to calculate
specific capacity (Fig. 6**e**). The NPPC-950 ZAB exhibited a higher
specific capacity of 800.1 mAh g$_{Zn}^{-1}$ than that of Pt/C ZAB (700.3
mAh g$_{Zn}^{-1}$), which suggested the excellent battery performance of
NPPC-950 ZAB could be ascribed to its high-efficiency ORR. In addi-
tion, NPPC-950 ZAB showed smooth voltage plateaus at different
current densities (Fig. 6**f**), and the first voltage plateau at 2 mA cm^{-2}
was 1.34 V. At the same time, the last was 1.33 V, a drop of only
0.75%, indicating its superior rate performance. The long-term
rechargeability of NPPC-950 ZAB was evaluated by continuous gal-
vanostatic charging-discharging at a current density of 5 mA cm^{-2}
and 20 min per cycle. The identical amounts of RuO$_2$ were mixed
with NPPC-950 and Pt/C to ensure their charging capability. As
shown in Fig. 6**g**, the NPPC-950 + RuO$_2$ ZAB exhibited a lower volt-
age gap and steadily operated for 300 h with negligible gap
increase, whereas the Pt/C + RuO$_2$ ZAB output a continuously
increasing voltage gap. This further demonstrated its outstanding

anti-polarization ability during the charge/discharge process and
promising application prospect in ZAB.

To demonstrate wearable electronic devices performance, we
self-assembled a solid-state flexible ZAB with NPPC-950 as the
cathode material, as shown in Fig. 7**a**. It is noted that the OCV of
the prepared flexible ZAB reached 1.46 V (Fig. 7**b**). Due to the high
viscosity and low ionic conductivity of the solid electrolyte [52],
the open-circuit voltage of a solid-state flexible battery is usually
lower than that of an aqueous battery. Fig. 7**c** depicts the charge
and corresponding power density graphs of NPPC-950-based flex-
ible ZAB, which attained a power density of 50.1 mW cm^{-2}. More-
over, an assembled flexible ZAB lets light up an LED board (Fig. 7**d**).
NPPC-950-based flexible ZAB in Fig. 7**e** exhibited stable voltage
plateaus in the galvanostatic current discharge quiz for current
densities from 2 to 15 mA cm^{-2}, demonstrating its excellent rate
performance. To investigate the cycling stability of such flexible
ZAB, we conducted a charge/discharge test at 5 mA cm^{-2} for
10 min per cycle (Fig. 7**f**), which proved that it could charge and
discharge continuously and stably for more than 5 h. Finally, the
flexible ZAB was bent to different degrees, yet its open-circuit volt-
age remained generally stable (Fig. 7**g**).

As discussed above, the excellent ORR catalytic activity of NPPC-
950 may originate from the following aspects: (1) The MOF-
derived three-dimensional carbon skeleton possessed a huge
specific surface area and abundant mesopores, which contributed
to a faster mass transfer [53]. (2) The introduction of N/P heteroa-
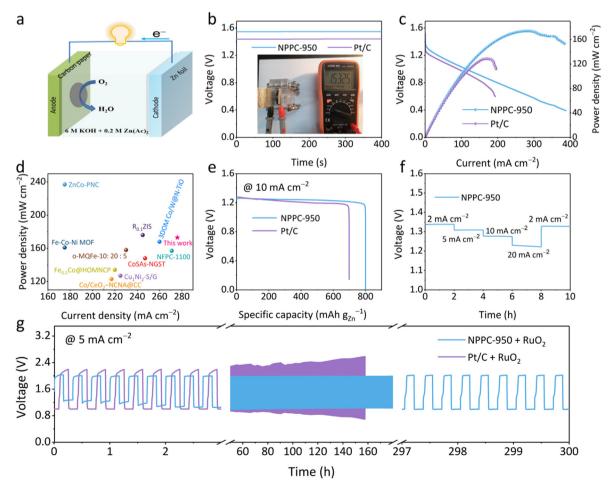toms reduced the work function of NPPC-950, which may be attrib-

Fig. 6. (a) Model drawing of a ZAB unit. (b) Open circuit voltage (OCV) curves of NPPC-950 and Pt/ C ZAB. (c) Discharge polarization curves and power density diagrams of NPPC-950 and Pt/ C ZAB. (d) Comparison of the ZAB performance for NPPC-950 and other reported catalysts. (e) Specific capacity of NPPC-950 and Pt/C ZAB. (f) Voltage platform of NPPC-950 ZAB at different discharge current densities. (g) Charge-discharge curves of NPPC-950 + RuO$_2$ and Pt/C + RuO$_2$ ZAB at 5 mA cm^{-2} (20 min per cycle).
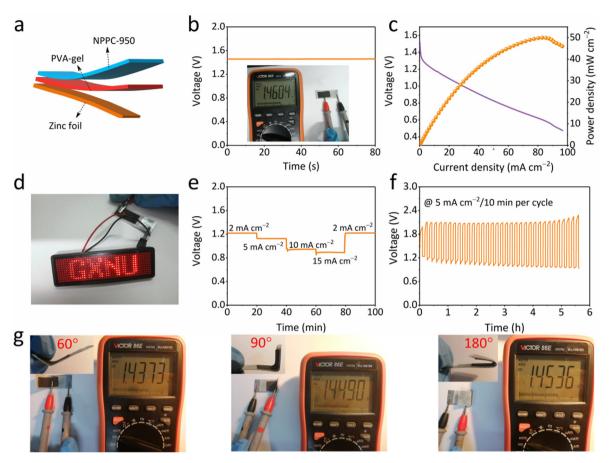
Fig. 7. (a) Model drawing of a flexible ZAB. (b) OCV curve of NPPC-950-based flexible ZAB. (c) Discharge polarization curves and power density diagrams of NPPC-950-based flexible ZAB. (d) LED lighting demonstration of NPPC-950-based flexible ZAB. (e) Voltage platform of NPPC-950-based flexible ZAB at different discharge current densities. (f) Charge-discharge curves of NPPC-950-based flexible ZAB at 5 mA cm^{-2}. (g) OCV at different bending angles.

uted to the incorporation of heteroatoms that changed the electronic properties of the carbon material, thus contributing to the electron transfer from the active sites to the adsorbed oxygen [45]. (3) The co-doping synergistically promoted the catalytic activity, in addition, the P—C bond changed the charge and spin density of the C atom, which provided more active sites [54].

4. Conclusion

A novel N/P co-doped porous carbon catalyst (NPPC) was prepared via a high-temperature red phosphorus phosphating process. The endogenous nitrogen doping was achieved during the first calcination utilizing the nitrogen in the ZIF-8 ligand. Secondly, exogenous phosphorus doping was conducted during the second co-calcination with red phosphorus. Two-step calculations increased the carbon material's graphitization and enabled the zinc element's complete evaporation. Benefiting from the three-dimensional geometry of ZIF-8, the resulting catalyst featured a large specific surface area. In addition, such a phosphating method was easy to operate and avoided introducing unnecessary elements. The P element maintained an ultra-low doping level but significantly reduced the surface work function of NPPC-950 while enhancing the ORR activity. Experimental results indicated that NPPC-950 possessed promising oxygen reduction activity, excellent stability and resistance to methanol in alkaline solutions. XPS analysis after stability testing showed that the stable existence of the P—C bond and pyrrolic-N are critical factors for stable ORR performance. Furthermore, aqueous and solid-state flexible zinc air battery tests demonstrated its favourable potential for real-world applications.

In short, we have created a novel phosphorus doping method with the advantages of simple operation, uniform doping and stable product structure. The technique can be extended to the preparation of phosphorus-doped different types of carbon materials for applications.

CRediT authorship contribution statement

Chuan Hu: Conceptualization, Writing – original draft. **Qinrui Liang:** Investigation. **Yuting Yang:** Data curation. **Qiming Peng:** Methodology. **Zuyang Luo:** Data curation. **Jiaxin Dong:** Supervision. **Tayirjan Taylor Isimjan:** Writing – review & editing. **Xiulin Yang:** Supervision, Writing – review & editing.

Data availability

No data was used for the research described in the article.

Declaration of Competing Interest

The authors declare that they have no known competing financial interests or personal relationships that could have appeared to influence the work reported in this paper.

Acknowledgements

the Project of High-Level Talents of Guangxi (F-KA18015), and Guangxi Technology Base and Talent Subject (GUIKE AD18126001, GUIKE AD20297039).

Appendix A. Supplementary material

Supplementary data to this article can be found online at https://doi.org/10.1016/j.jcis.2022.11.118.

References

[1] M. Li, K. Wang, Q. Lv, N, P-co-Doped Graphdiyne as Efficient Metal-free Catalysts for Oxygen Reduction Reaction, Chem. Res. Chin. Univ. 37 (2021) 1283–1288, https://doi.org/10.1007/s40242-021-1256-6.

[2] T. Wang, A. Chutia, D.J.L. Brett, P.R. Shearing, G. He, G. Chai, I.P. Parkin, Palladium alloys used as electrocatalysts for the oxygen reduction reaction, Energy Environ. Sci. 14 (2021) 2639–2669, https://doi.org/10.1039/d0ee03915b.

[3] H. Han, Y. Wang, Y. Zhang, Y. Cong, J. Qin, R. Gao, C. Chai, Y. Song, Oxygen Reduction Reaction Electrocatalysts Derived from Metalloporphyrin-Modified Meso-/Macroporous Polyaniline, Acta Phys. -Chim. Sin. 37 (2021) 2008017, https://doi.org/10.3866/pku.Whxb202008017.

[4] Z. Lyu, X.G. Zhang, Y. Wang, K. Liu, C. Qiu, X. Liao, W. Yang, Z. Xie, S. Xie, Amplified Interfacial Effect in an Atomically Dispersed RuO_x-on-Pd 2D Inverse Nanocatalyst for High-Performance Oxygen Reduction, Angew. Chem. Int. Ed. 60 (2021) 16093–16100, https://doi.org/10.1002/anie.202104013.

[5] J. Guan, Y. Zan, R. Shao, J. Niu, M. Dou, B. Zhu, Z. Zhang, F. Wang, Phase Segregated $Pt-SnO_2$/C Nanohybrids for Highly Efficient Oxygen Reduction Electrocatalysis, Small 16 (2020) e2005048, http://doi.org/10.1002/smll.202005048.

[6] S. Li, Z.Q. Tian, Y. Liu, Z. Jang, S.W. Hasan, X. Chen, P. Tsiakaras, P.K. Shen, Hierarchically skeletal multi-layered Pt-Ni nanocrystals for highly efficient oxygen reduction and methanol oxidation reactions, Chin. J. Catal. 42 (2021) 648–657, https://doi.org/10.1016/s1872-2067(20)63680-4.

[7] J. Guan, S. Yang, T. Liu, Y. Yu, J. Niu, Z. Zhang, F. Wang, Intermetallic FePt@PtBi Core-Shell Nanoparticles for Oxygen Reduction Electrocatalysis, Angew. Chem. Int. Ed. 60 (2021) 21899–21904, https://doi.org/10.1002/anie.202107437.

[8] H. Nan, Y.-Q. Su, C. Tang, R. Cao, D. Li, J. Yu, Q. Liu, Y. Deng, X. Tian, Engineering the electronic and strained interface for high activity of PdMcore@Ptmonolayer electrocatalysts for oxygen reduction reaction, Sci Bull. 65 (2020) 1396–1404, https://doi.org/10.1016/j.scib.2020.04.015.

[9] J. Zhu, A.O. Elnabawy, Z. Lyu, M. Xie, E.A. Murray, Z. Chen, W. Jin, M. Mavrikakis, Y. Xia, Facet-controlled Pt–Ir nanocrystals with substantially enhanced activity and durability towards oxygen reduction, Mater. Today 35 (2020) 69–77, https://doi.org/10.1016/j.mattod.2019.11.002.

[10] Q. Lai, Y. Zhao, Y. Liang, J. He, J. Chen, In Situ Confinement Pyrolysis Transformation of ZIF-8 to Nitrogen-Enriched Meso-Microporous Carbon Frameworks for Oxygen Reduction, Adv. Funct. Mater. 26 (2016) 8334–8344, https://doi.org/10.1002/adfm.201603607.

[11] X. Zhang, X. Xu, S. Yao, C. Hao, C. Pan, X. Xiang, Z.Q. Tian, P.K. Shen, Z. Shao, S.P. Jiang, Boosting Electrocatalytic Activity of Single Atom Catalysts Supported on Nitrogen-Doped Carbon through N Coordination Environment Engineering, Small 18 (2022) 2105329, https://doi.org/10.1002/smll.202105329.

[12] X. Xu, C. Su, Z. Shao, Fundamental Understanding and Application of $Ba_{0.5}Sr_{0.5}Co_{0.8}Fe_{0.2}O_{3-\delta}$ Perovskite in Energy Storage and Conversion: Past, Present, and Future, Energy Fuels 35 (2021) 13585–13609, https://doi.org/10.1021/acs.energyfuels.1c02111.

[13] X. Xu, Y. Pan, Y. Zhong, C. Shi, D. Guan, L. Ge, Z. Hu, Y.-Y. Chin, H.-J. Lin, C.-T. Chen, H. Wang, S.P. Jiang, Z. Shao, New Undisputed Evidence and Strategy for Enhanced Lattice-Oxygen Participation of Perovskite Electrocatalyst through Cation Deficiency Manipulation, Adv. Sci. 9 (2022) 2200530, https://doi.org/10.1002/advs.202200530.

[14] L. Yang, J. Shui, L. Du, Y. Shao, J. Liu, L. Dai, Z. Hu, Carbon-Based Metal-Free ORR Electrocatalysts for Fuel Cells: Past, Present, and Future, Adv. Mater. 31 (2019) 1804799, https://doi.org/10.1002/adma.201804799.

[15] D. Yan, Y. Li, J. Huo, R. Chen, L. Dai, S. Wang, Defect Chemistry of Nonprecious-Metal Electrocatalysts for Oxygen Reactions, Adv. Mater. 29 (2017) 1606459, https://doi.org/10.1002/adma.201606459.

[16] H. Shi, Y. Shen, F. He, Y. Li, A. Liu, S. Liu, Y. Zhang, Recent advances of doped carbon as non-precious catalysts for oxygen reduction reaction, J. Mater. Chem. A 2 (2014) 15704–15716, https://doi.org/10.1039/C4TA02790F.

[17] C. Tang, Q. Zhang, Nanocarbon for Oxygen Reduction Electrocatalysis: Dopants, Edges, and Defects, Adv. Mater. 29 (2017) 1604103, https://doi.org/10.1002/adma.201604103.

[18] G. Ren, S. Chen, J. Zhang, N. Zhang, C. Jiao, H. Qiu, C. Liu, H.-L. Wang, N-doped porous carbon spheres as metal-free electrocatalyst for oxygen reduction reaction, J. Mater. Chem. A 9 (2021) 5751–5758, https://doi.org/10.1039/d0ta11493f.

[19] Z. Xing, R. Jin, X. Chen, B. Chen, J. Zhou, B. Tian, Y. Li, D. Fan, Self-templating construction of N, P-co-doped carbon nanosheets for efficient eletreocatalytic oxygen reduction reaction, Chem. Eng. J. 410 (2021) https://doi.org/10.1016/j.cej.2020.128015 128015.

[20] X. Zhang, X. Wen, C. Pan, X. Xiang, C. Hao, Q. Meng, Z.Q. Tian, P.K. Shen, S.P. Jiang, N species tuning strategy in N, S co-doped graphene nanosheets for electrocatalytic activity and selectivity of oxygen redox reactions, Chem. Eng. J. 431 (2022), https://doi.org/10.1016/j.cej.2021.133216 133216.

[21] Y.-N. Sun, J. Yang, X. Ding, W. Ji, A. Jaworski, N. Hedin, B.-H. Han, Synergetic contribution of nitrogen and fluorine species in porous carbons as metal-free and bifunctional oxygen electrocatalysts for zinc–air batteries, Appl. Catal. B: Environ. 297 (2021), https://doi.org/10.1016/j.apcatb.2021.120448 120448.

[22] H. Zhao, Z.-P. Hu, Y.-P. Zhu, L. Ge, Z.-Y. Yuan, P-doped mesoporous carbons for high-efficiency electrocatalytic oxygen reduction, Chin. J. Catal. 40 (2019) 1366–1374, https://doi.org/10.1016/S1872-2067(19)63363-2.

[23] F. Kong, X. Cui, Y. Huang, H. Yao, Y. Chen, H. Tian, G. Meng, C. Chen, Z. Chang, J. Shi, N-Doped Carbon Electrocatalyst: Marked ORR Activity in Acidic Media without the Contribution from Metal Sites?, Angew Chem. Int. Ed. 61 (2022) e202116290, https://doi.org/10.1002/anie.202116290.

[24] M. Liu, M. Yang, X. Shu, J. Zhang, Design Strategies for Carbon-Based Electrocatalysts and Application to Oxygen Reduction in Fuel Cells, Acta Phys. -Chim. Sin. 37 (2021) 2007072, https://doi.org/10.3866/pku.Whxb202007072.

[25] H.B. Yang, J. Miao, S.-F. Hung, J. Chen, H.B. Tao, X. Wang, L. Zhang, R. Chen, J. Gao, H.M. Chen, L. Dai, B. Liu, Identification of catalytic sites for oxygen reduction and oxygen evolution in N-doped graphene materials: Development of highly efficient metal-free bifunctional electrocatalyst, Sci. Adv. 2 (2016) e1501122, https://doi.org/10.1126/sciadv.1501122.

[26] L. Yang, S. Jiang, Y. Zhao, L. Zhu, S. Chen, X. Wang, Q. Wu, J. Ma, Y. Ma, Z. Hu, Boron-Doped Carbon Nanotubes as Metal-Free Electrocatalysts for the Oxygen Reduction Reaction, Angew. Chem. Int. Ed. 50 (2011) 7132–7135, https://doi.org/10.1002/anie.201101287.

[27] X. Zhu, C. Hu, R. Amal, L. Dai, X. Lu, Heteroatom-doped carbon catalysts for zinc–air batteries: progress, mechanism, and opportunities, Energy Environ. Sci. 13 (2020) 4536–4563, https://doi.org/10.1039/d0ee02800b.

[28] X. Zhang, Z. Lu, Z. Fu, Y. Tang, D. Ma, Z. Yang, The mechanisms of oxygen reduction reaction on phosphorus doped graphene: A first-principles study, J. Power Sources 276 (2015) 222–229, https://doi.org/10.1016/j.jpowsour.2014.11.105.

[29] X. Feng, Y. Bai, M. Liu, Y. Li, H. Yang, X. Wang, C. Wu, Untangling the respective effects of heteroatom-doped carbon materials in batteries, supercapacitors and the ORR to design high performance materials, Energy Environ. Sci. 14 (2021) 2036–2089, https://doi.org/10.1039/D1EE00166C.

[30] X. Xue, H. Yang, T. Yang, P. Yuan, Q. Li, S. Mu, X. Zheng, L. Chi, J. Zhu, Y. Li, J. Zhang, Q. Xu, N, P-coordinated fullerene-like carbon nanostructures with dual active centers toward highly-efficient multi-functional electrocatalysis for C_O2RR, ORR and Zn-air battery, J. Mater. Chem. A 7 (2019) 15271–15277, https://doi.org/10.1039/C9TA03828K.

[31] J. Tong, W. Ma, W. Wang, J. Ma, W. Li, L. Bo, H. Fan, Nitrogen/phosphorus dual-doped hierarchically porous graphitic biocarbon with greatly improved performance on oxygen reduction reaction in alkaline media, J. Electroanal. Chem. 809 (2018) 163–170, https://doi.org/10.1016/j.jelechem.2017.12.055.

[32] H. Jiang, Y. Wang, J. Hao, Y. Liu, W. Li, J. Li, N and P co-functionalized three-dimensional porous carbon networks as efficient metal-free electrocatalysts for oxygen reduction reaction, Carbon 122 (2017) 64–73, https://doi.org/10.1016/j.carbon.2017.06.043.

[33] S. Huang, Y. Meng, Y. Cao, S. He, X. Li, S. Tong, M. Wu, N-, O- and P-doped hollow carbons: Metal-free bifunctional electrocatalysts for hydrogen evolution and oxygen reduction reactions, Appl. Catal. B: Environ. 248 (2019) 239–248, https://doi.org/10.1016/j.apcatb.2019.01.080.

[34] C. Zhang, L. Hou, C. Cheng, Z. Zhuang, F. Zheng, W. Chen, Nitrogen and Phosphorus Co-doped Hollow Carbon Spheres as Efficient Metal-Free Electrocatalysts for the Oxygen Reduction Reaction, ChemElectroChem 5 (2018) 1891–1898, https://doi.org/10.1002/celc.201800045.

[35] K. Yuan, D. Lützenkirchen-Hecht, L. Li, L. Shuai, Y. Li, R. Cao, M. Qiu, X. Zhuang, M.K.H. Leung, Y. Chen, U. Scherf, Boosting Oxygen Reduction of Single Iron Active Sites via Geometric and Electronic Engineering: Nitrogen and Phosphorus Dual Coordination, J. Am. Chem. Soc. 142 (5) (2020) 2404–2412, https://doi.org/10.1021/jacs.9b11852.

[36] Z.H. Wang, H.H. Jin, T. Meng, K. Liao, W.Q. Meng, J.L. Yang, D.P. He, Y.L. Xiong, S.C. Mu, Fe, Cu-Coordinated ZIF-Derived Carbon Framework for Efficient Oxygen Reduction Reaction and Zinc-Air Batteries, Adv. Funct. Mater. 28 (2018) 1802596, https://doi.org/10.1002/adfm.201802596.

[37] Z.J. Zhu, H.J. Yin, Y. Wang, C.H. Chuang, L. Xing, M.Y. Dong, Y.R. Lu, G. Casillas-Garcia, Y.L. Zheng, S. Chen, Y.H. Dou, P.R. Liu, Q.L. Cheng, H.J. Zhao, Coexisting Single-Atomic Fe and Ni Sites on Hierarchically Ordered Porous Carbon as a Highly Efficient ORR Electrocatalyst, Adv. Mater. 32 (2020) 2004670, https://doi.org/10.1002/adma.202004670.

[38] Q. He, Y. Meng, H. Zhang, Y. Zhang, Q. Sun, T. Gan, H. Xiao, X. He, H. Ji, Amino-metalloporphyrin polymers derived Fe single atom catalysts for highly efficient oxygen reduction reaction, Sci China Chem 63 (2020) 810–817, https://doi.org/10.1007/s11426-019-9703-7.

[39] Y. Cai, L. Tao, G. Huang, N. Zhang, Y. Zou, S. Wang, Regulating carbon work function to boost electrocatalytic activity for the oxygen reduction reaction, Chin. J. Catal. 42 (2021) 938–944, https://doi.org/10.1016/S1872-2067(20)63701-9.

[40] R. Hao, J. Chen, Z. Wang, Y. Huang, P. Liu, Y. Jan, K. Liu, C. Liu, Z. Lu, Trimetallic Zeolitic imidazolite framework-derived Co nanoparticles@CoFe-nitrogen-doped porous carbon as bifunctional electrocatalysts for Zn-air battery, J. Colloid Interface Sci. 586 (2021) 621–629, https://doi.org/10.1016/j.jcis.2020.10.130.

[41] G. Zhu, H. Yang, Y. Jiang, Z. Sun, X. Li, J. Yang, H. Wang, R. Zou, W. Jiang, P. Qiu, W. Luo, Modulating the Electronic Structure of FeCo Nanoparticles in N-Doped Mesoporous Carbon for Efficient Oxygen Reduction Reaction, Adv Sci. 9 (2022) 2200394, https://doi.org/10.1002/advs.202200394.

[42] Z. Yan, Y. Zhang, Z. Jiang, D. Jiang, W. Wei, Z. Hu, Nitrogen-Doped Bimetallic Carbide-Graphite Composite as Highly Active and Extremely Stable Electrocatalyst for Oxygen Reduction Reaction in Alkaline Media, Adv. Funct. Mater. 32 (2022) 2204031, https://doi.org/10.1002/adfm.202204031.

[43] X. Cai, L. Lai, L. Zhou, Z. Shen, Durable Freestanding Hierarchical Porous Electrode for Rechargeable Zinc-Air Batteries, ACS Appl. Energy Mater. 2 (2019) 1505–1516, https://doi.org/10.1021/acsaem.8b02101.

[44] J.P. Paraknowitsch, Y. Zhang, B. Wienert, A. Thomas, Nitrogen- and phosphorus-co-doped carbons with tunable enhanced surface areas promoted by the doping additives, Chem. Commun. 49 (2013) 1208–1210, https://doi.org/10.1039/c2cc37398j.

[45] J. Zhu, M. Xiao, P. Song, J. Fu, Z. Jin, L. Ma, J. Ge, C. Liu, Z. Chen, W. Xing, Highly polarized carbon nano-architecture as robust metal-free catalyst for oxygen reduction in polymer electrolyte membrane fuel cells, Nano Energy 49 (2018) 23–30, https://doi.org/10.1016/j.nanoen.2018.04.021.

[46] X. Tang, R. Cao, L. Li, B. Huang, W. Zhai, K. Yuan, Y. Chen, Engineering efficient bifunctional electrocatalysts for rechargeable zinc–air batteries by confining Fe–Co–Ni nanoalloys in nitrogen-doped carbon nanotube@nanosheet frameworks, J. Mater. Chem. A 8 (2020) 25919–25930, https://doi.org/10.1039/D0TA09580J.

[47] L. Li, S. Shen, G. Wei, J. Zhang, Electrocatalytic Activity of Hemin-Derived Hollow Non-Precious Metal Catalyst for Oxygen Reduction Reaction, Acta Phys. -Chim. Sin. 37 (2021) 1911011, https://doi.org/10.3866/pku.Whxb201911011.

[48] Y. Jiao, Y. Zheng, M. Jaroniec, S.Z. Qiao, Design of electrocatalysts for oxygen- and hydrogen-involving energy conversion reactions, Chem. Soc. Rev. 44 (2015) 2060–2086, https://doi.org/10.1039/C4CS00470A.

[49] G. Liu, X. Xia, C. Zhao, X. Zhang, W. Zhang, Ultrafine Ni nanoparticles anchored on carbon nanofibers as highly efficient bifunctional air electrodes for flexible solid-state zinc-air batteries, J. Colloid Interface Sci. 588 (2021) 627–636, https://doi.org/10.1016/j.jcis.2020.11.053.

[50] Y. Zhu, X. Wang, J. Shi, L. Gan, B. Huang, L. Tao, S. Wang, Neuron-inspired design of hierarchically porous carbon networks embedded with single-iron sites for efficient oxygen reduction, Sci China Chem 65 (2022) 1445–1452, https://doi.org/10.1007/s11426-022-1285-y.

[51] Y. Mun, S. Lee, K. Kim, S. Kim, S. Lee, J.W. Han, J. Lee, Versatile Strategy for Tuning ORR Activity of a Single Fe-N_4 Site by Controlling Electron-Withdrawing/Donating Properties of a Carbon Plane, J. Am. Chem. Soc. 141 (2019) 6254–6262, https://doi.org/10.1021/jacs.8b13543.

[52] J. Fu, Z. Paul-Cano, M. Gyu-Park, A.P. Yu, M. Fowler, Z.W. Chen, Electrically Rechargeable Zinc-Air Batteries: Progress, Challenges, and Perspectives, Adv. Mater. 29 (2017) 1604685, https://doi.org/10.1002/adma.201604685.

[53] S.S.A. Shah, T. Najam, J. Yang, M.S. Javed, L. Peng, Z. Wei, Modulating the microenvironment structure of single Zn atom: ZnN4P/C active site for boosted oxygen reduction reaction, Chinese, J. Catal. 43 (2022) 2193–2201, https://doi.org/10.1016/s1872-2067(22)64089-0.

[54] Y. Liao, H. Chen, C. Ou, L. Bao, R. Li, H. Liu, N, P co-doped graphene enriched phosphorus as a highly efficient oxygen reduction catalyst, J. Electroanal. Chem. 921 (2022), https://doi.org/10.1016/j.jelechem.2022.116560 116560.